Supplementary Information (SI) for Journal of Materials Chemistry A.

Supporting Information

High-Yield Dehydration Synthesis of Biomass Hard Carbon for Sustainable Sodium-Ion Batteries

Wenjing Xu, ‡[abc] Zhangliu Tian, ‡[a] Hui Bi, *[c] Meng Wang, [a] Zhuoran Lv, [c] YuSha Gao, [ab] Kun Liu, [a] Jiandong Zhang, [a] Fuqiang Huang,*[cde]

---

[a] *Shanghai Institute of Ceramics, Chinese Academy of Science, Shanghai 200050, China.*

[b] *Center of Materials Science and Optoelectronics Engineering, University of Chinese Academy of Science, Beijing 100049, China.*

[c] *Key Lab of Intelligent Creation for Extreme Energy Materials of Ministry of Education, School of Materials Science and Engineering, Shanghai Jiao Tong University, Dongchuan Road 800, 200240 Shanghai, China.*

[d] *School of Materials Science and Engineering and Zhang jiang Institute for Advanced Study, Shanghai Jiao Tong University, Shanghai, 200240, China*

[e] *Inner Mongolia Research Institute, Shanghai Jiao Tong University, Hohhot, 010010, China*

‡ These authors contributed equally to this work.

Methods

Synthesis of hard carbons

The 5 g of cotton was mixed with 30 ml of methanesulfonic acid. The mixture was reacted in an oil bath at 80°C for 5h under stirring at 300 rpm. During the reaction, the biomass dissolved rapidly and the color of the solution changed from clear to black. The reaction was then slowly quenched by adding deionized water until the system temperature no longer increased. The quenched reaction solutions were diafiltrated and rinsed with deionized water until the filtrate became neutral. The collected samples were dried in an oven at 100 °C. Subsequently, the obtained black powders were annealed at 1300 °C for 3 h under an argon (Ar) atmosphere with a heating rate of 5 °C min^{-1}, yielding the sample denoted as COT-MSA.

Under the same procedure, carbon materials were also prepared using wood, bamboo, cellulose, glucose, cyclodextrin, or polylactic acid (PLA) as precursors, which were labeled WOOD-MSA, BAM-MSA, CEL-MSA, GLU-MSA, CYC-MSA, and PLA-MSA, respectively. Notably, the PLA-derived sample was pyrolyzed at 1100 °C.

Material characterization

X-ray diffraction (XRD) patterns were collected on a Bruker D8 Advance diffractometer with Cu Kα radiation (λ=1.5406 Å). Raman spectroscopy was conducted on a Jobin-Yvon LabRAM HR-800 spectrometer with a laser excitation wavelength of 532 nm. Scanning electron microscopy (SEM) measurement was obtained through a JEOL (JSM6510) scanning electron microscope. Transmission electron microscopy (TEM) observations were carried out on a JEOL (JEM-2100F) transmission electron microscope. Surface composition and valence were studied by X-ray photoelectron spectra measurements (Thermo Scientific Escalab 250 X-ray photoelectron spectrometer). The Fourier transform infrared spectra (FTIR) was conducted by a spectrometer labelled as nicolet is 50. Nitrogen adsorption-desorption isotherms and pore size distribution was recorded on ASAP 2020 M (Micromeritics) under liquid nitrogen temperature. The small angle X-ray scattering (SAXS) was conducted by a spectator Pilatus 3R 1M (Xeuss 2.0). The thermogravimetric analysis (TGA) was done by PE STA8000 under Ar. The electric conductivity was determined by Malvern Mastersizer 2000. The hyphenation of TGA/FTIR/mass spectroscopy (MS) was conducted in PerKinElmer. The electron paramagnetic resonance (EPR) was completed by a Bruker EMX PLUS instrument.

Electrochemical Measurements

Electrodes were prepared by mixing active materials, carbon black (super P), and sodium alginate in a weight ratio of 8.5:1:0.5. Electrochemical performance was evaluated using 2032-type coin cells consisting of a Na metal anode, glass fiber separator (GF/D, Whatman), and an electrolyte of 1.0 mol L^{-1} $NaPF_6$ in diglyme. Galvanostatic cycling was performed using a LAND-CT2001A test system within a voltage window of 0.01-2.5 V (vs Na^+/Na) at a 0.1 C rate (30 mA g^{-1}). Charge-discharge and galvanostatic intermittent titration technique (GITT) tests were carried out on LAND-CT2001A test system at various current densities. GITT measurements were performed through a pulse current of 30 mA g^{-1} for 30 min, followed by relaxation intervals of 120 min. Cyclic voltammogram (CV) from 0.01 to 3.0 V and electrochemical impedance spectroscopy (EIS) over the frequency from 100 kHz to 0.1 Hz were measured by CHI760E electrochemical workstation (Chenhua, Shanghai). For 2032 coin-typed full-cells, a slurry of 80 wt% of $Na_4Fe_3(PO_4)_2P_2O_7$, 10 wt% of carbon black and 10 wt% of polyvinylidene difluoride was plated on Al foils as cathode. Neither the cathodes nor the anodes were presodiated before assembling the batteries. The electrolyte was 1.0 mol L^{-1} $NaPF_6$ in diglyme. The N/P ratio was ~1.2.

Life cycle assessment

Life cycle assessment was conducted based on the ISO 14040:2006 guideline by using open LCA software and Ecoinvent database. Life cycle impact assessment was performed based on CML v4.8 (2016) methodology and considered five main environmental impact categories including global warming potential, acidification potential, eutrophication potential, human toxicity potential, and ozone depletion potential.

Correlated Calculations

Interlayer spacing (d (002)): d (002) was calculated using Bragg's equation:

$$d_{002} = \frac{n\lambda}{2\sin\theta} \qquad \text{(S1)}$$

Layer stacking distance (Lc) and longitudinal size of structural elements (La) were calculated according to the formula (Scherrer equation):

$$Lc\&La = \frac{k\lambda}{\beta cos\theta} \qquad (2)$$

where, k is scherrer constant (k = 0.9 for Lc and k = 1.84 for La), λ is the radiation wavelength, β is the half-height width of the (002) reflection, θ is the reflection angle of (002) or (100). The number of layers in a stack was calculated using given formula:

$$n = \frac{Lc}{d_{002}} + 1 \qquad (3)$$

Diameter of the closed nanopore: Based on the SAXS test results, the closed pores were quantitatively analyzed using the fitting model as equation:

$$\left(I_Q\right) = \frac{A}{Q^x} + \frac{Ba_0^4}{\left(1 + a_0^2Q^2\right)^2} + D \qquad (4)$$

where A and B are proportional to the total surface area of the large and small pores, respectively. Q is the scattering vector, and D is a constant background term. The length, a_0, is the characteristic length over which electron density variations occur. The diameter of the closed nanopore (R') can be calculated using the value of a_0, as shown in the equation:

$$R^{'} = 2a_0\sqrt{10} \qquad (5)$$

Capacitive contribution to the capacity: This can be quantified by separating the response current (i) into diffusion-controlled and capacitive-controlled components at a specific potential (v). The equation is given as:

$$i = k_1 v + k_2 v^{0.5} \qquad (6)$$

where k_1 corresponds to the capacitive control, and $k_2 v^{0.5}$ corresponds to the diffusion control. This relationship allows the capacitive contribution to the total capacity in the CV profile to be quantified.

Diffusion coefficients calculations: The sodium ion diffusion coefficients ($D_{Na}{}^{+}$) are calculated based on the following formula:

$$D_{Na^+} = \frac{4}{\pi\tau}\left(\frac{n_m V_m}{S}\right)\left(\frac{\Delta E_S}{\Delta E_\tau}\right)^2 \qquad (7)$$

where τ displays the constant current pulse time, n_m and V_m, are the molar number and molar volume of active material, respectively. S is the contact area of the electrode−electrolyte interface. ΔE_s and ΔE_t represent the IR drop and the potential difference in a constant current pulse during the cycling process.

Supplementary Fig.s 1-43

Fig. S1: Flow chart for the methanesulfonic acid treatment of biomass. Acidolysis of cotton in MSA generates molecules with extended conjugated systems, imparting a purple color to the solution. Subsequent deep dehydration of the cotton into carbonaceous material results in a color change of the solution to black.

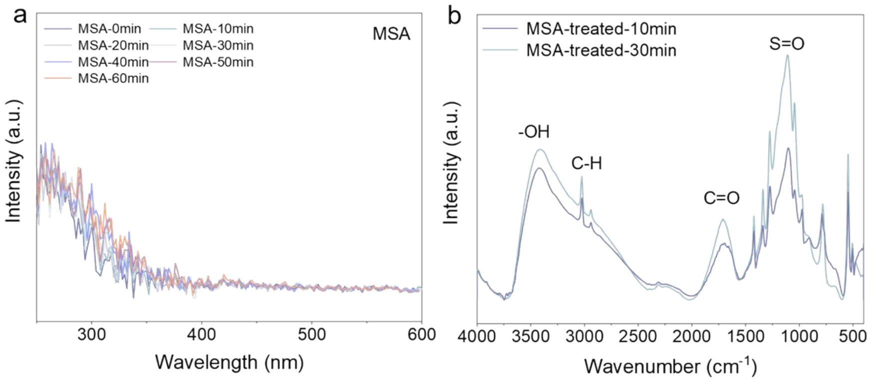

Fig. S2: (a) In situ UV-Vis spectra of neat MSA at different heating times. (b) FTIR spectra of the samples treated with MSA for 10 min and 30 min. At 10 min, when cellulose starts to dissolve, its characteristic peaks are intense. After 30 min, these peaks decrease as most of the cellulose dissolves. Concurrently, the MSA peaks weaken due to interference from small molecules in the liquid phase.

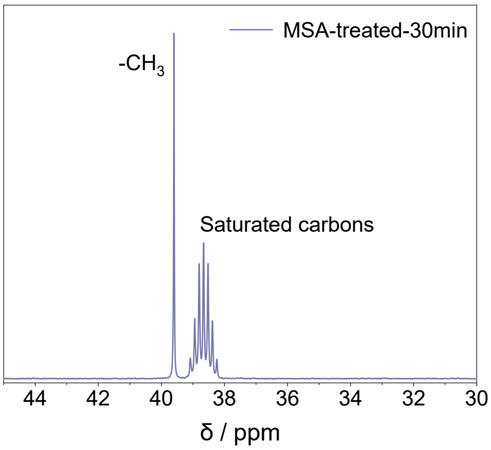

Fig. S3: (a)^{13}C NMR spectrum of the sample treated with MSA for 30min. After 30 min, the cellulose in the liquid phase decomposes into small-molecule saturated aliphatic carbons.

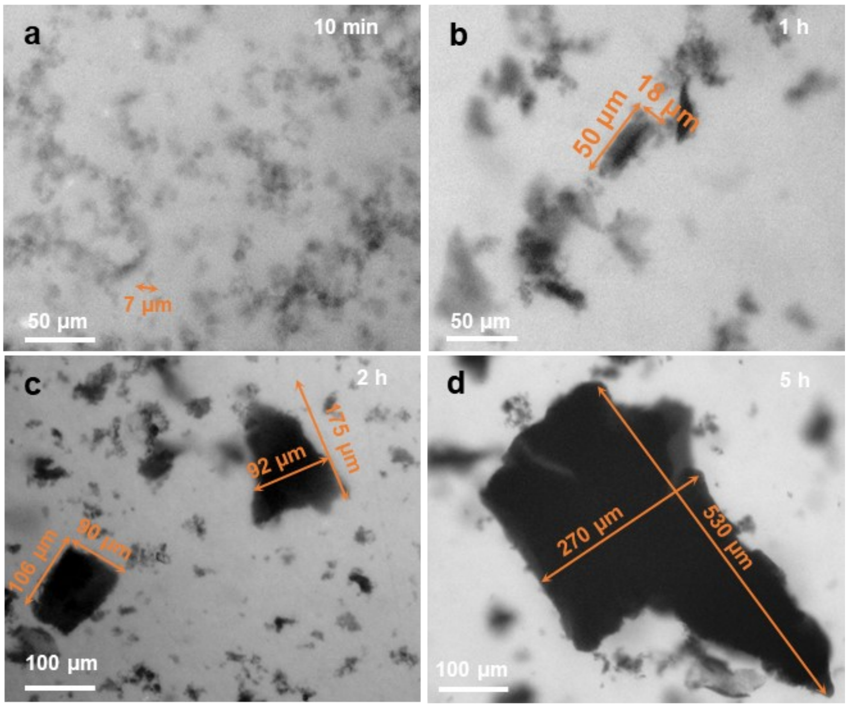

Fig. S4: Carbon cluster growth process. Images of the samples treated with MSA for (a) 10 min, (b) 1 h, (c) 2 h, and (d) 5h, respectively. At 10 min, cellulose is observed to be dissolving. After 1 h, the small molecules generated during the initial dissolution undergo further dehydration and aggregate through cross-linking. As dehydration progresses, the resulting carbon clusters continue to cross-link and grow.

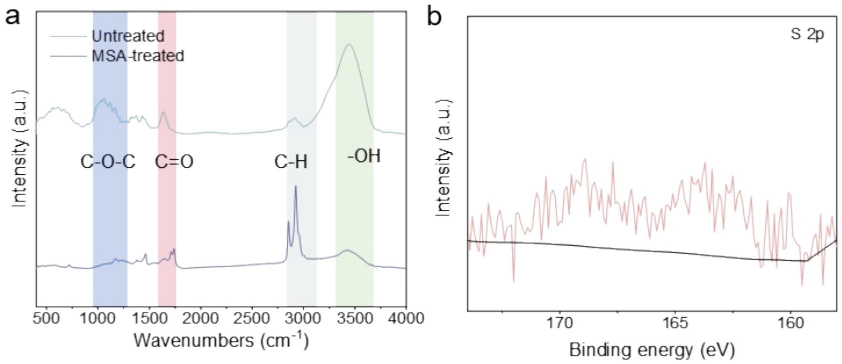

Fig. S5: (a) FTIR spectra of untreated and acid-treated cotton. After treatment with MSA, the cellulose framework is completely disrupted. (b) High-resolution S 2p XPS spectrum of the MSA-treated precursor.

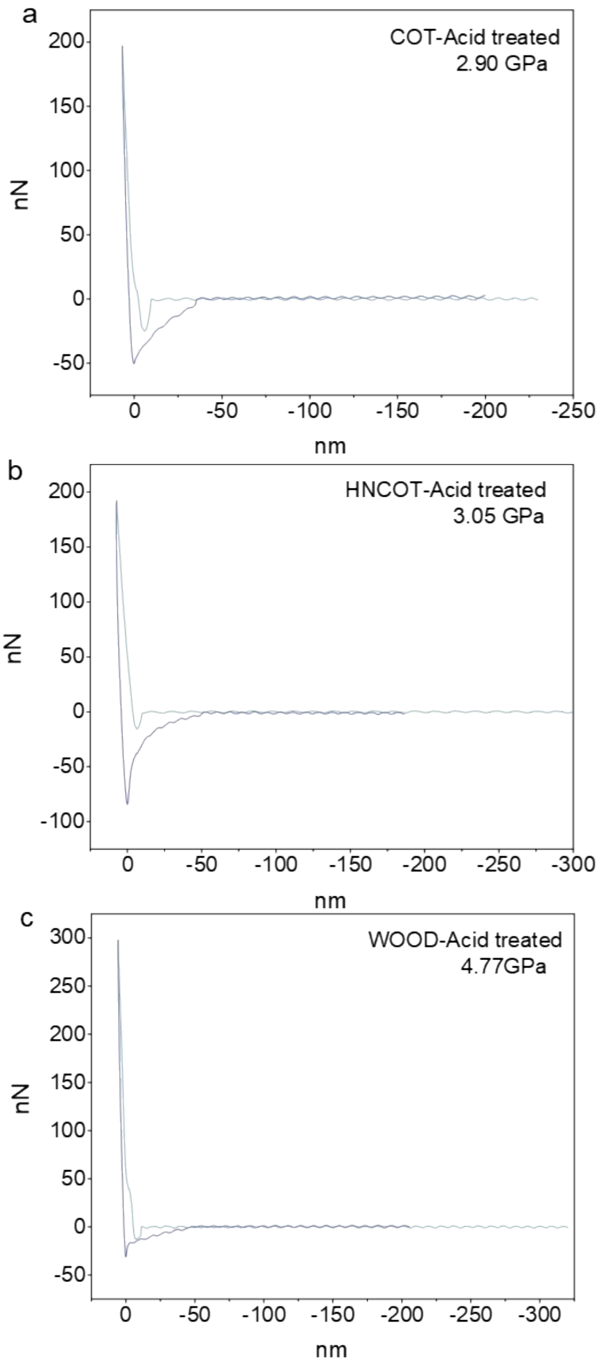

Fig. S6: Young's modulus of different biomasses after MSA treatment. (a) Cotton from Anhui, (b) cotton from Henan, and (c) wood. The results demonstrate that the materials treated with MSA exhibit similar mechanical properties and uniform characteristics.

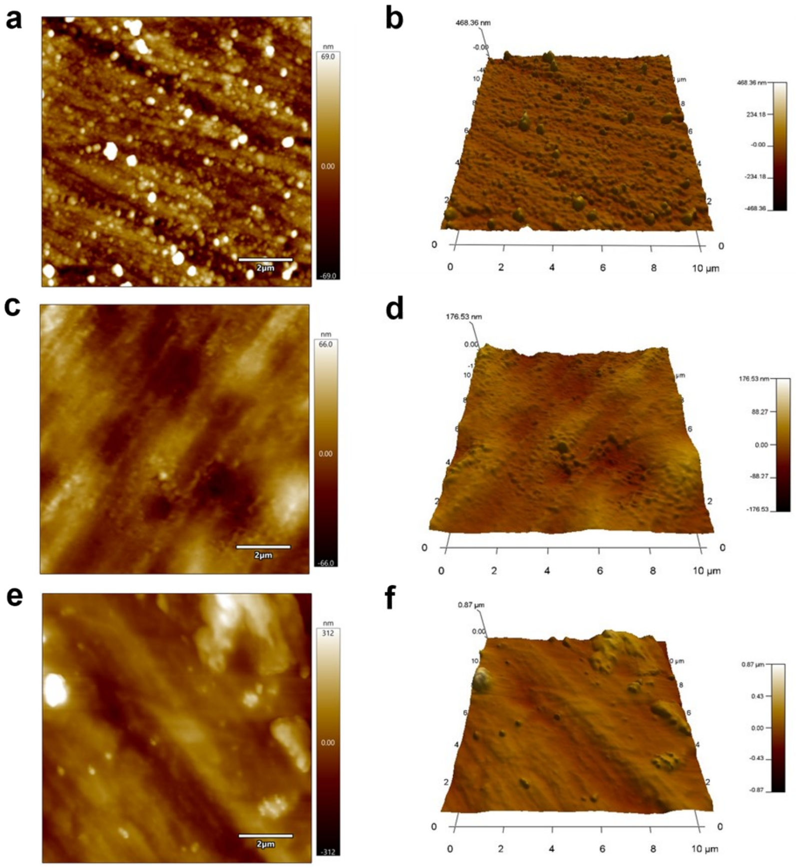

Fig. S7: Atomic force microscopy (AFM) images of the samples prepared for Young's modulus measurement. (a, b) Cotton from Anhui, (c, d) cotton from Henan, and (e, f) wood. AFM characterization of these samples reveals uniform and smooth morphologies.

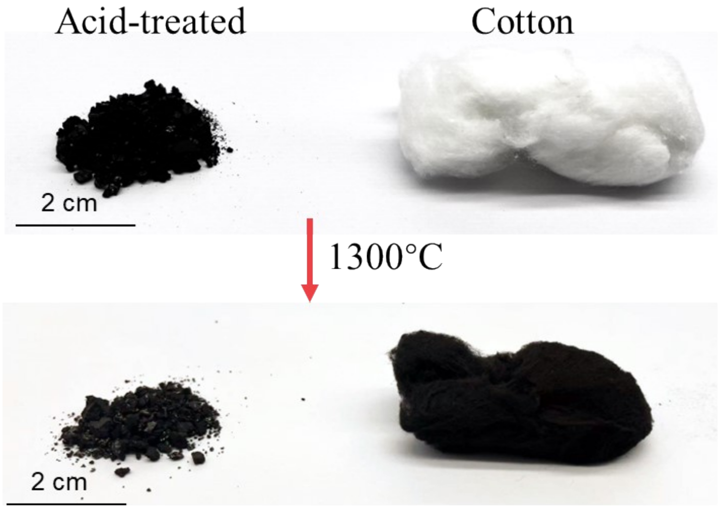

Fig. S8: Photographs of the samples before and after pyrolysis.

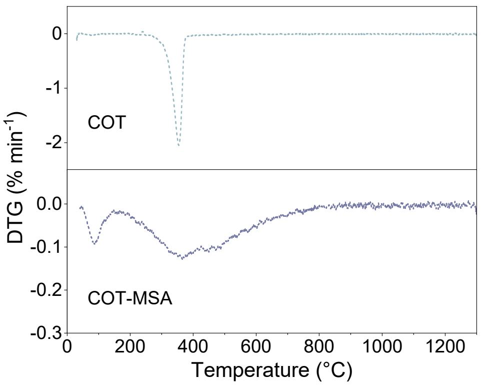

Fig. S9: DTG profiles of COT and COT-MSA. COT exhibits a concentrated and rapid weight loss, whereas COT-MSA undergoes a relatively slow weight loss. This slower weight loss behavior favors the formation of a stable carbon framework.

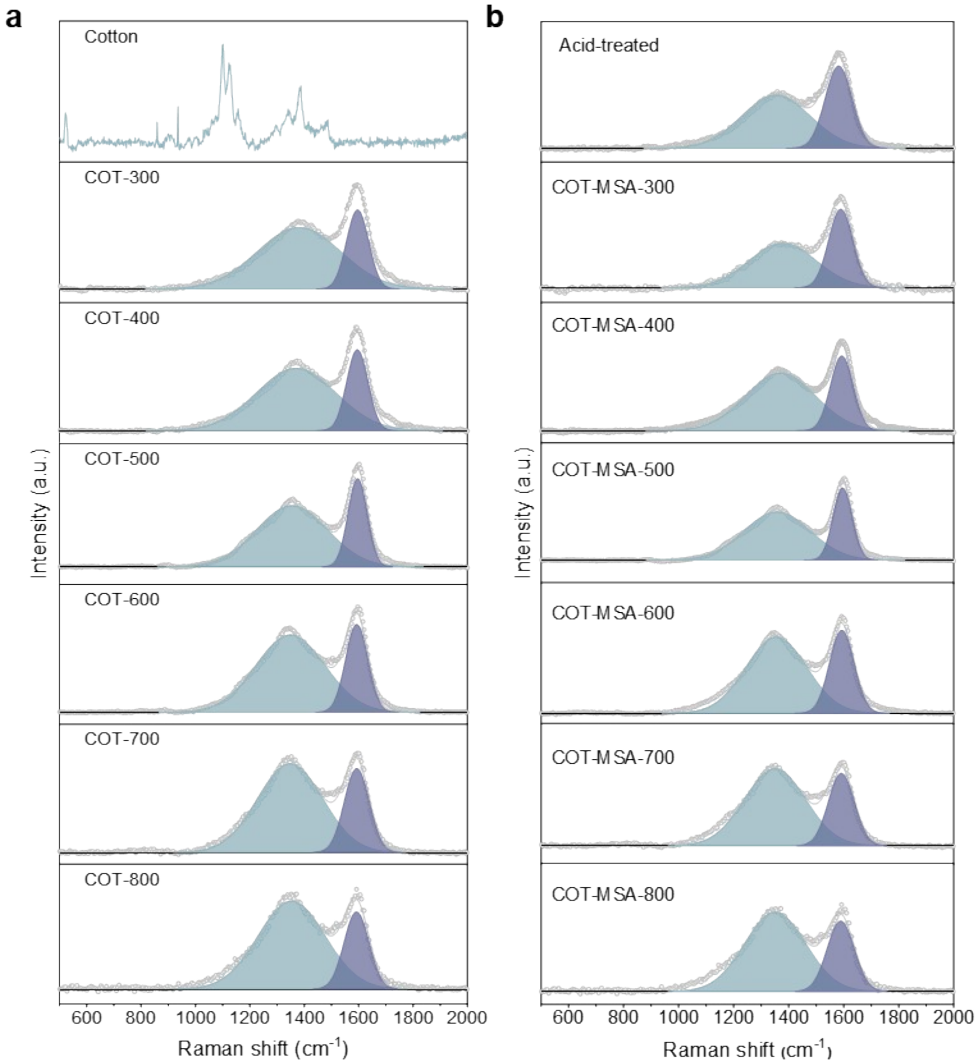

Fig. S10: Raman spectra of (a) COT and (b) COT-MSA under different Pyrolysis temperatures.

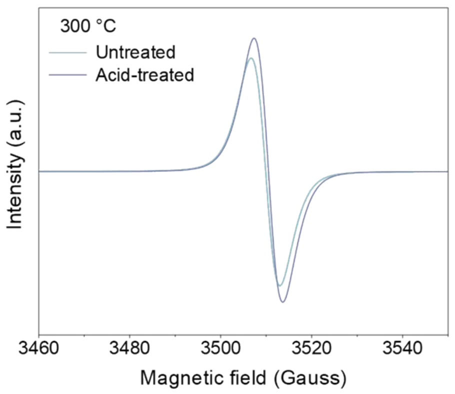

Fig. S11: EPR spectra of the samples with and without acid treatment after heating to 300°C.

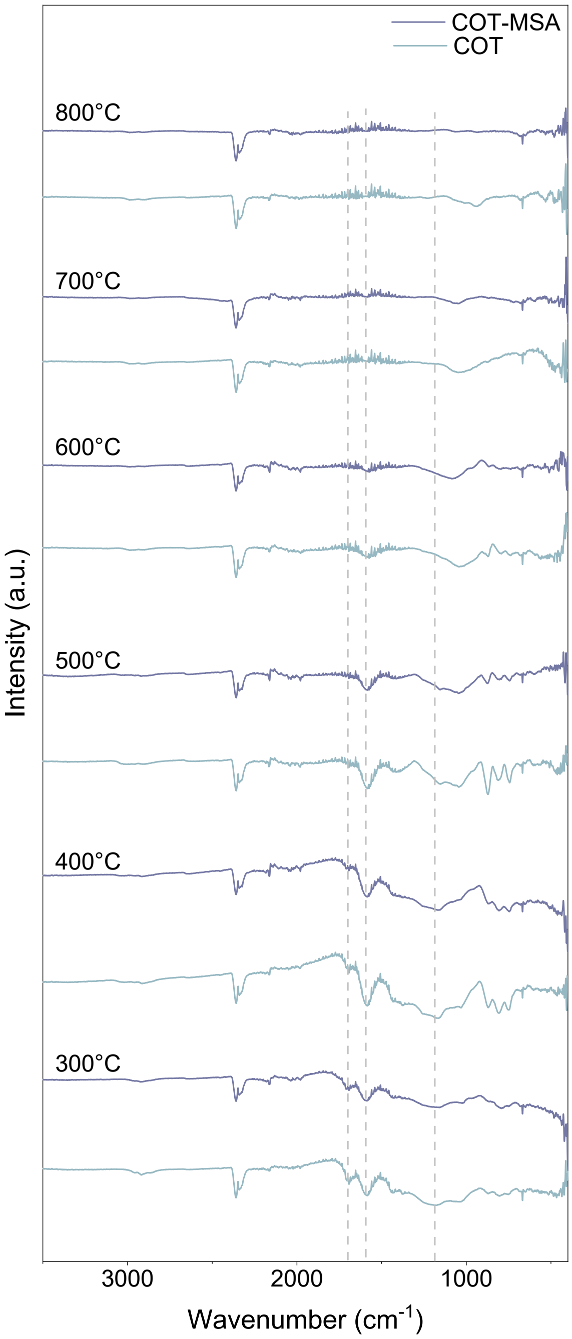

Fig. S12: FT-IR spectra of the COT and COT-MSA samples under different Pyrolysis temperatures. At different temperatures, the peak shapes of COT-MSA are generally smoother, whereas the COT sample exhibits a rapid change in peak intensity. This observation indicates that the MSA-treated material exhibits greater stability during pyrolysis.

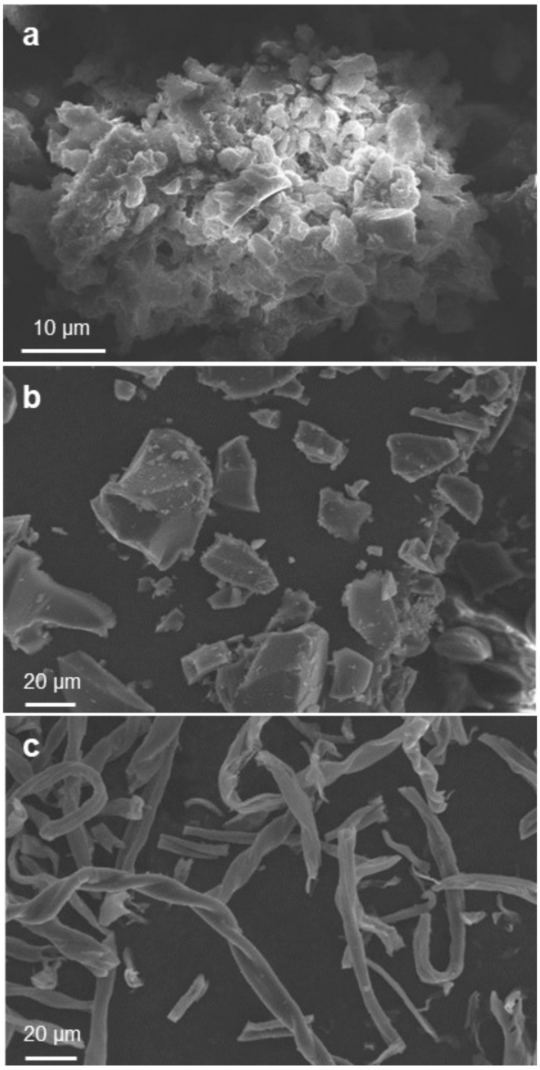

Fig. S13: Comparison of sample morphologies. SEM images of (a) acid-treated sample, (b) COT-MSA sample, and (c) COT sample.

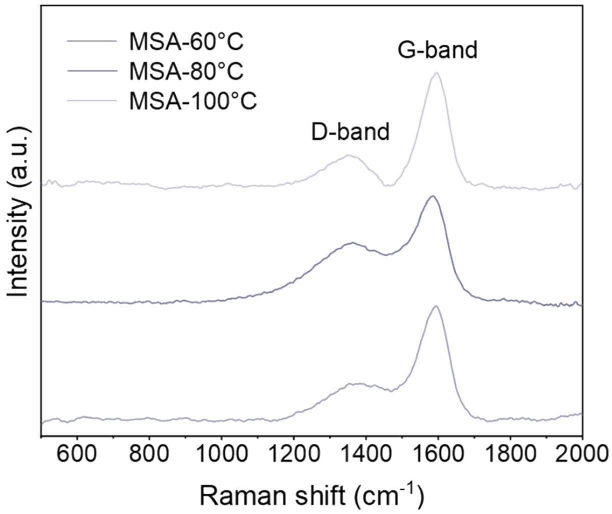

Fig. S14: Raman spectra of cotton subjected to MSA treatment at different temperatures. The results indicate that the sample treated at 80 °C exhibits a higher degree of order, suggesting that this temperature facilitates the rearrangement of carbon layers during subsequent pyrolysis.

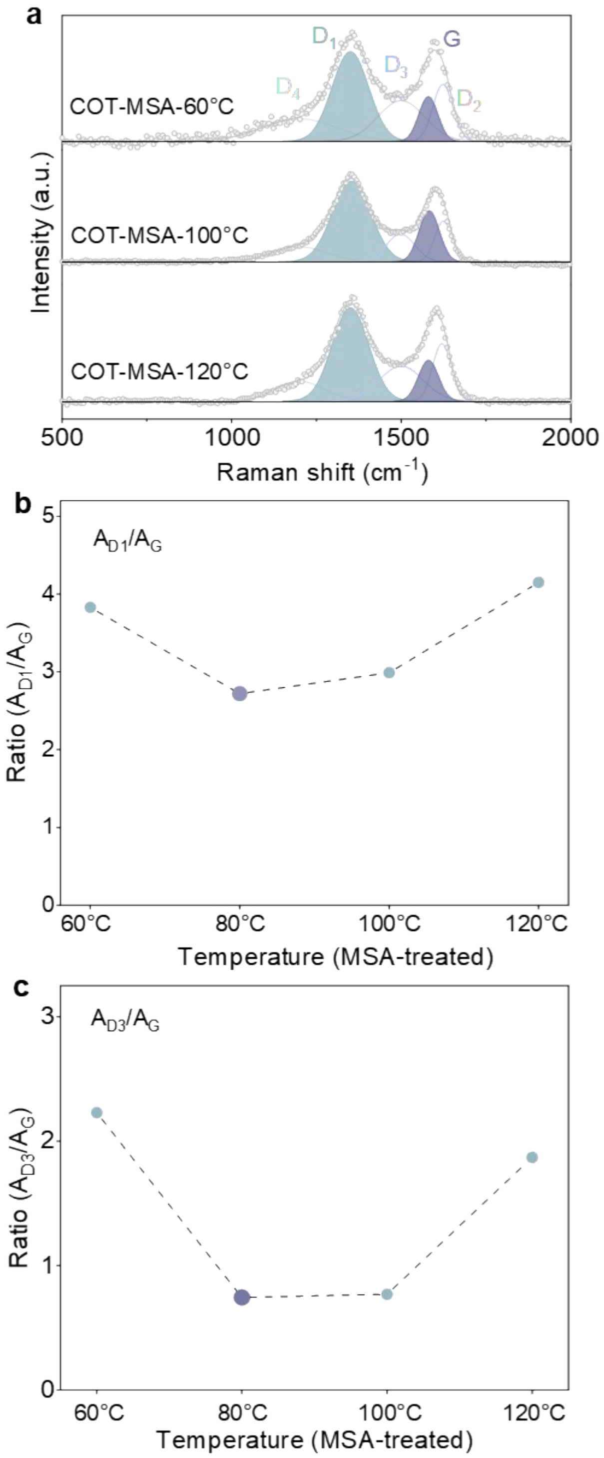

Fig. S15: Summary of Raman data for pyrolyzed samples with different MSA treatment temperatures. (a) Raman spectra of pyrolyzed samples (b) A_{D1}/A_G and (c) A_{D2}/A_G ratios extracted from Raman spectra of samples with different MSA treatment temperatures.

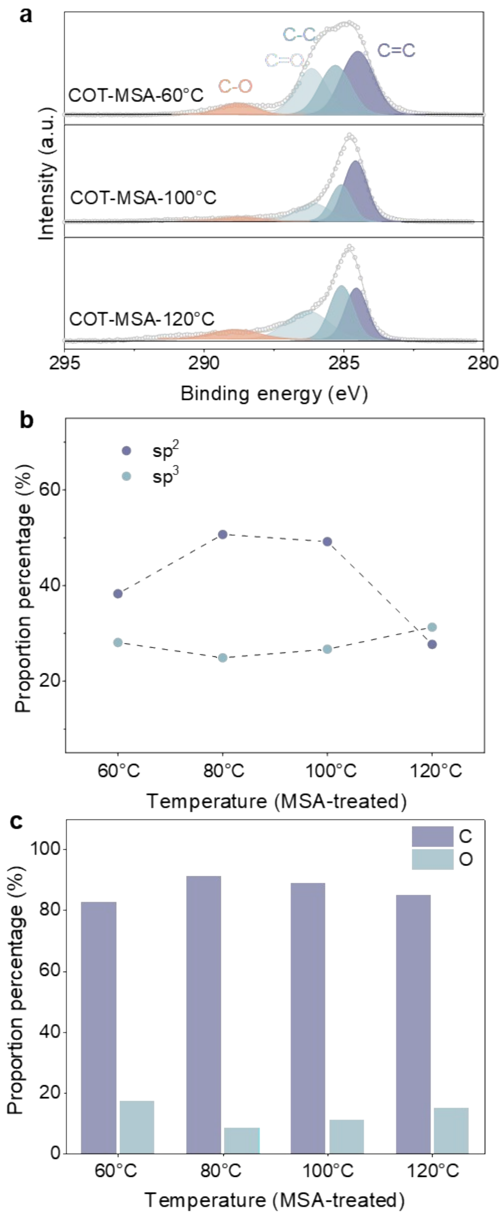

Fig. S16: Summary of XPS data for pyrolyzed samples with different MSA treatment temperatures. (a) C 1s XPS spectra of pyrolyzed samples (b) Variation in the proportions of sp^2 and sp^3 carbon as a function of MSA treatment temperature. (c) Proportions of carbon and oxygen contents in pyrolyzed samples under different MSA treatment temperatures.

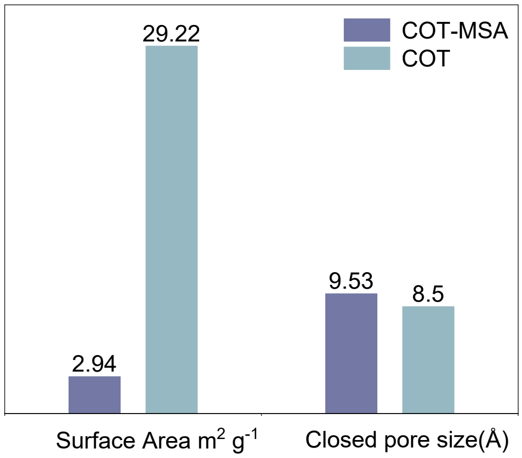

Fig. S17: Surface area and closed pore size of COT and COT-MSA. MSA treatment endows biomass-derived materials with a lower specific surface area and larger closed-pore size, a structural feature that contributes to the enhancement of overall electrochemical performance.

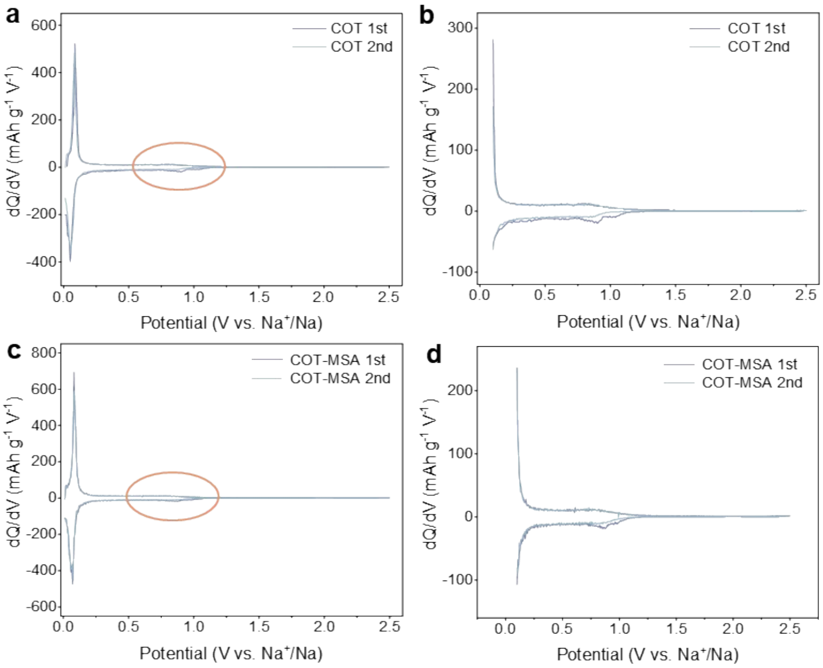

Fig. S18: Differential capacity analysis. dQ/dV curves of the first two charge–discharge cycles for (a, b) COT and (c, d) COT-MSA, and the corresponding enlarged views of the orange-highlighted regions shown in (b) and (d), respectively.

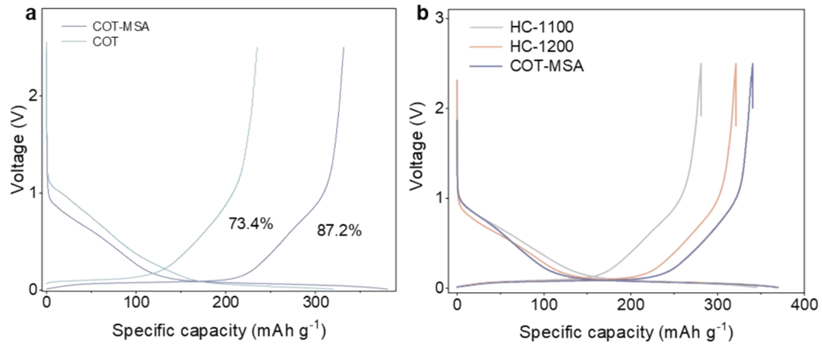

Fig. S19: (a) Initial charge/discharge profiles of COT and COT-MSA in ester-based electrolyte. The first discharge/charge curves for acid-treated sample with different pyrolysis temperature. Low carbonization temperatures result in incomplete pyrolysis, which prevents the full formation of closed-pore structures and thereby impairs specific capacity.

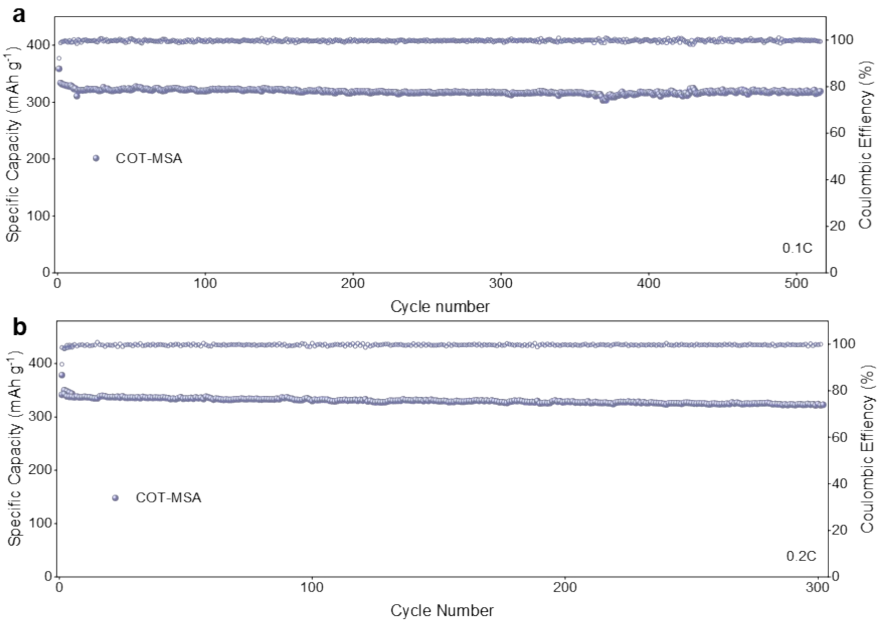

Fig. S20: Cycling performance of COT-MSA at (a) 0.1C and (b) 0.2C for half-cells. The stable carbon framework facilitates the stable operation of batteries under deep charge–discharge conditions.

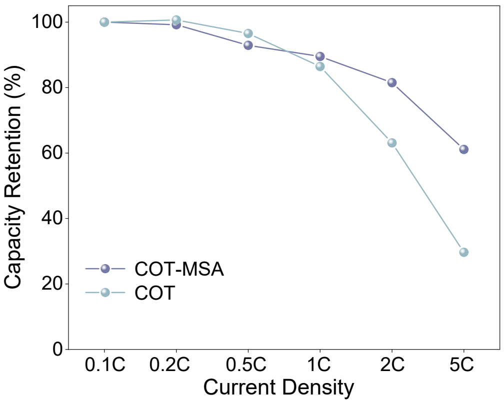

Fig. S21: Capacity retention of COT and COT-MSA. When the current density reaches 5C, COT-MSA exhibits a much higher capacity retention rate than COT, indicating that this structure has greater adaptability under high current density conditions.

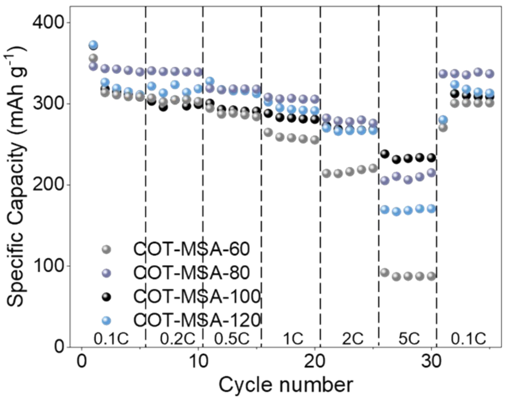

Fig. S22: Rate performance of acid-treated samples with different treatment temperatures. Among these, the material treated at 80°C exhibits the most prominent comprehensive performance.

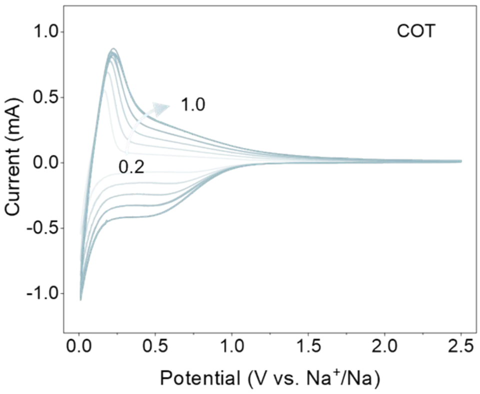

Fig. S23: CV curves of COT at different scan rates. The COT sample exhibits poor electrochemical stability.

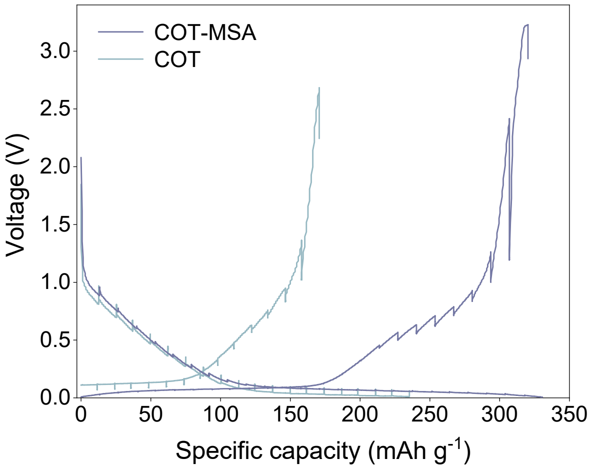

Fig. S24: Charge and discharge profiles of COT and COT-MSA in the second cycle at 30 mAh g^{-1}.

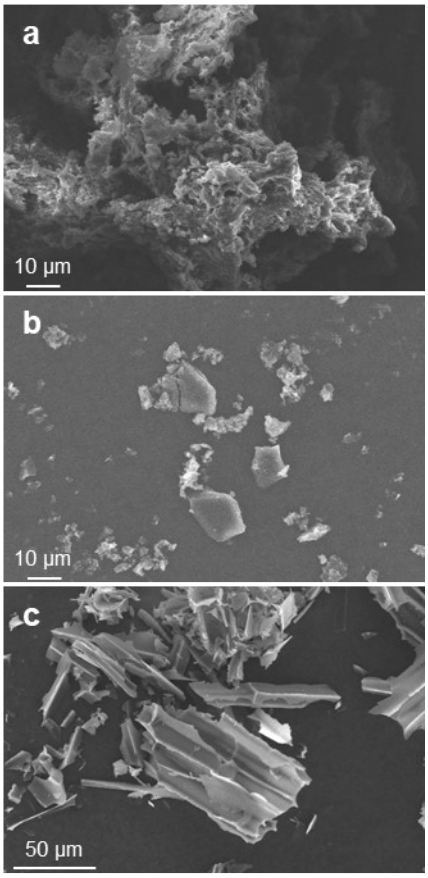

Fig. S25: Morphological comparison of wood with different treatment. SEM images of (a) acid-treated wood, (b) acid-treated wood at 1300 °C, and (c) directly pyrolyzed wood. MSA-pretreated biomass features densely stacked small carbon clusters, which upon pyrolysis evolve into carbon particles with sizes ranging from tens to hundreds of micrometers. By contrast, biomass subjected to direct pyrolysis largely preserves its original morphology.

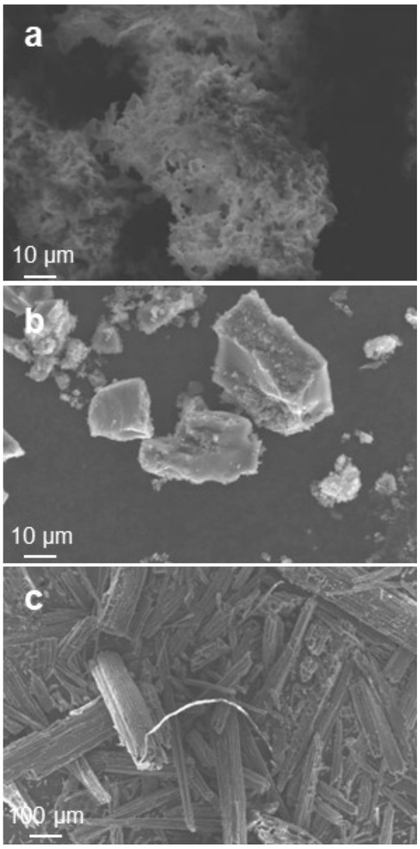

Fig. S26: Morphological comparison of bamboo with different treatment. SEM images of (a) acid-treated bamboo, (b) acid-treated bamboo at 1300 °C, and (c) directly pyrolyzed bamboo.

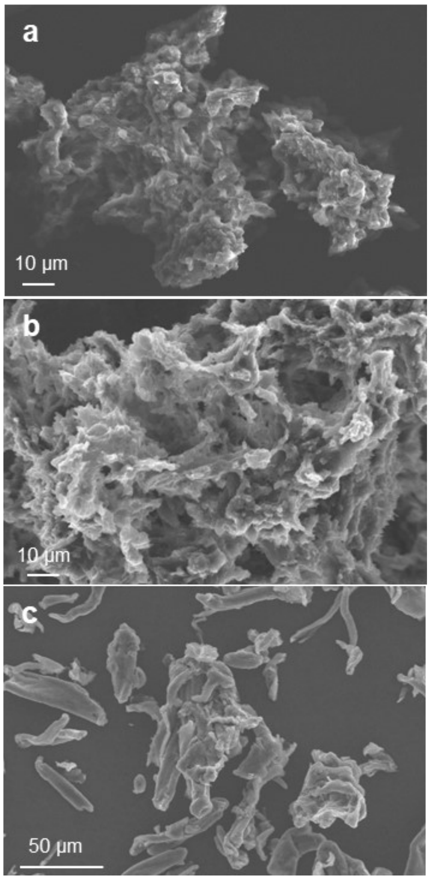

Fig. S27: Morphological comparison of cellulose with different treatment. SEM images of (a) acid-treated cellulose, (b) acid-treated cellulose at 1300 °C, and (c) directly pyrolyzed cellulose.

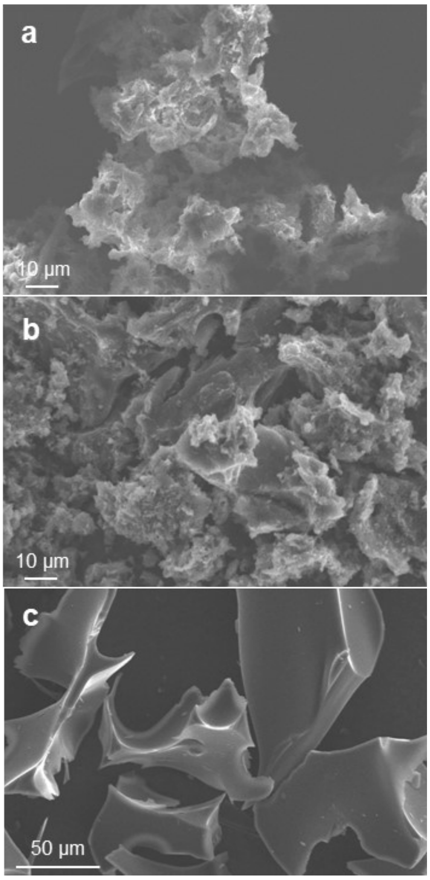

Fig. S28: Morphological comparison of glucose with different treatment. SEM images of (a) acid-treated glucose, (b) acid-treated glucose at 1300 °C, and (c) directly pyrolyzed glucose. When polysaccharide compounds are subjected to direct pyrolysis, large amounts of volatile gases are rapidly released; as these gases are rapidly escaped from the interior of the precursor, the carbon-based framework is expanded, and an expanded sheet-like structure is thereby formed.

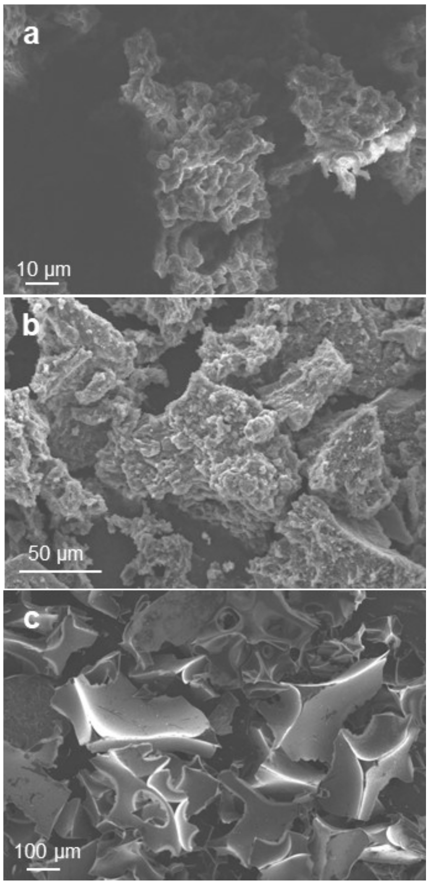

Fig. S29: Morphological comparison of cyclodextrin with different treatment. SEM images of (a) acid-treated cyclodextrin, (b) acid-treated cyclodextrin at 1300 °C, and (c) directly pyrolyzed cyclodextrin.

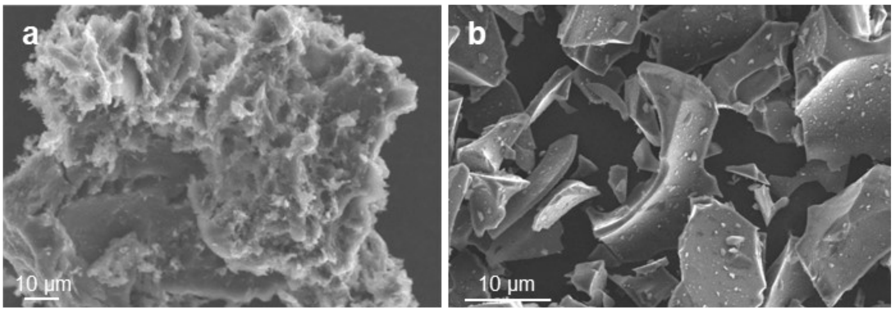

Fig. S30: Morphological comparison of PLA with different treatment. SEM images of (a) acid-treated PLA and (b) acid-treated PLA at 1300 °C. PLA has a relatively high oxygen content; under high-temperature pyrolysis, it undergoes deep oxidation and cracking, resulting in no solid carbon residue.

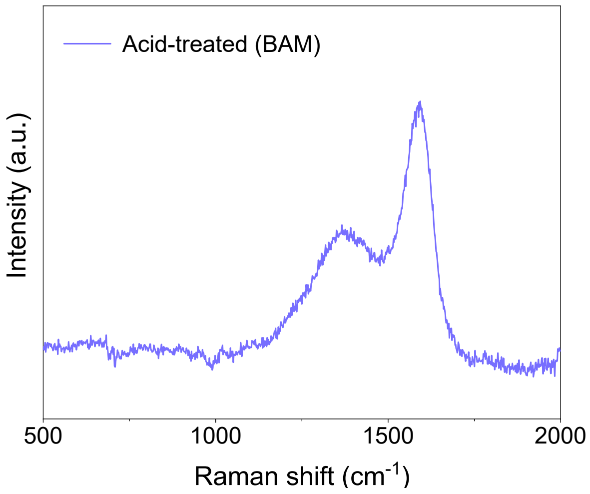

Fig. S31: Raman spectrum of acid-treated bamboo. All materials treated with MSA exhibit characteristic Raman bands associated with amorphous carbon.

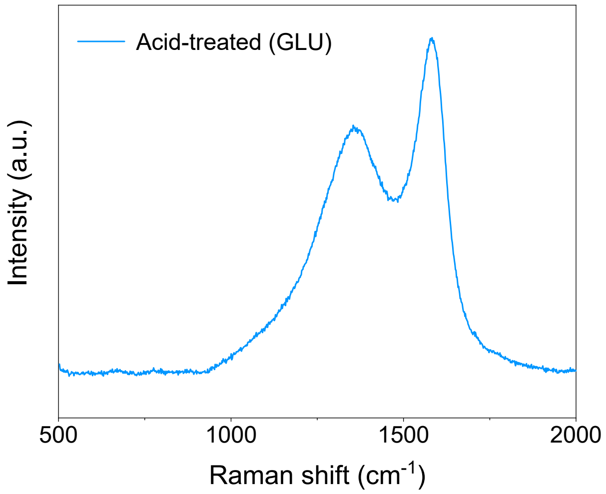

Fig. S32: Raman spectrum of acid-treated glucose.

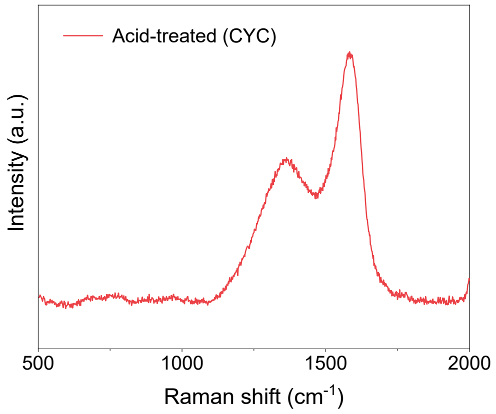

Fig. S33: Raman spectrum of acid-treated cyclodextrin.

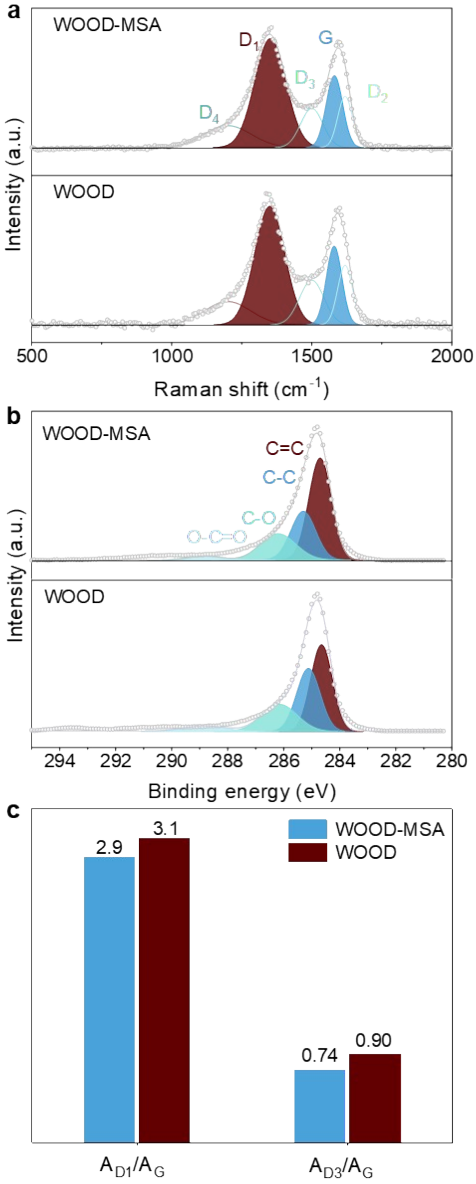

Fig. S34: Summary of structural data for pyrolyzed wood samples. (a) Raman and (b) XPS results for WOOD and WOOD-MSA. (c) Comparison of A_{D3}/A_G and A_{D1}/A_G ratios from Raman spectra between WOOD and WOOD-MSA.

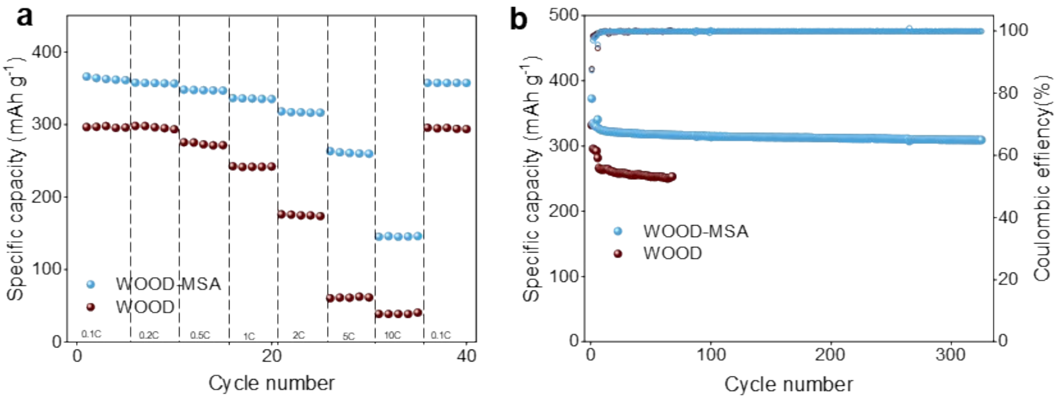

Fig. S35: (a) Rate performance and (b) cycling performance of WOOD and WOOD-MSA at 1C for half-cells. Materials treated with MSA exhibit superior comprehensive performance.

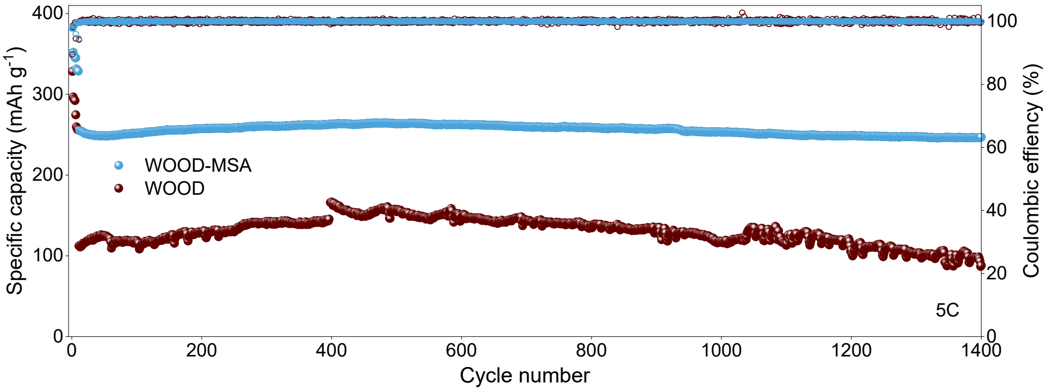

Fig. S36: Cycling performance of WOOD and WOOD-MSA at 5C for half-cells.

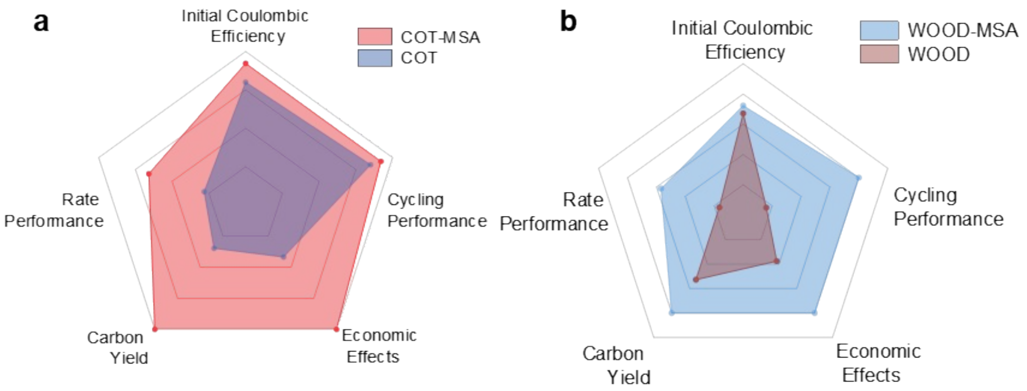

Fig. S37: Radar comparison charts of (a) cotton and (b) wood for various electrochemical properties and battery performance metrics. Materials treated with MSA demonstrate enhanced value across multiple dimensions.

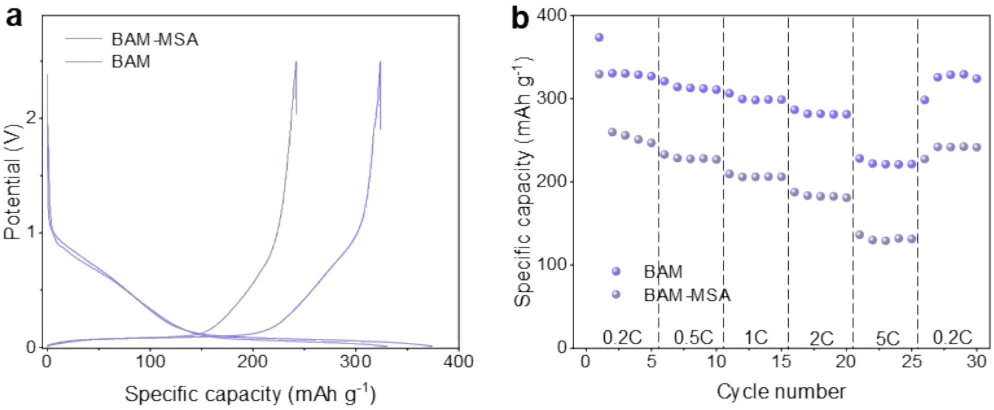

Fig. S38: Comparison of (a) the first discharge/charge curves and (b) rate performance for BAM and BAM-MSA in half cells.

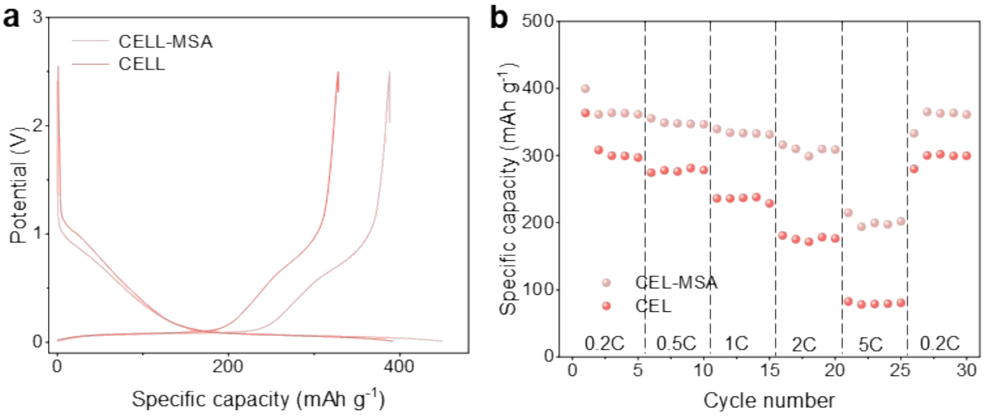

Fig. S39: Comparison of (a) the first discharge/charge curves and (b) rate performance for CELL and CELL-MSA in half cells.

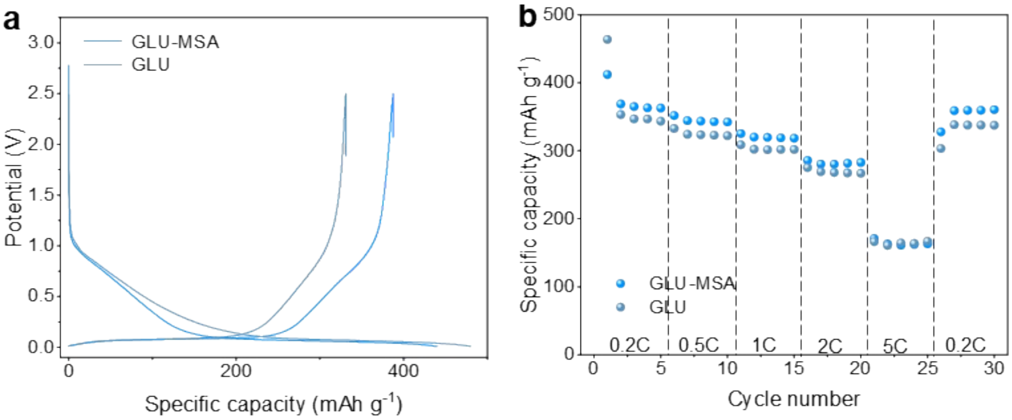

Fig. S40: Comparison of (a) the first discharge/charge curves and (b) rate performance for GLU and GLU-MSA in half cells.

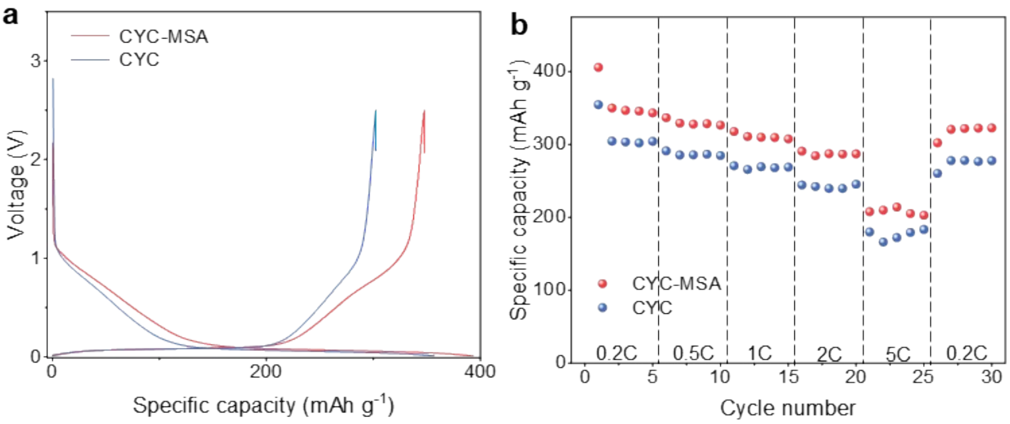

Fig. S41: Comparison of (a) the first discharge/charge curves and (b) rate performance for CYC and CYC-MSA in half cells.

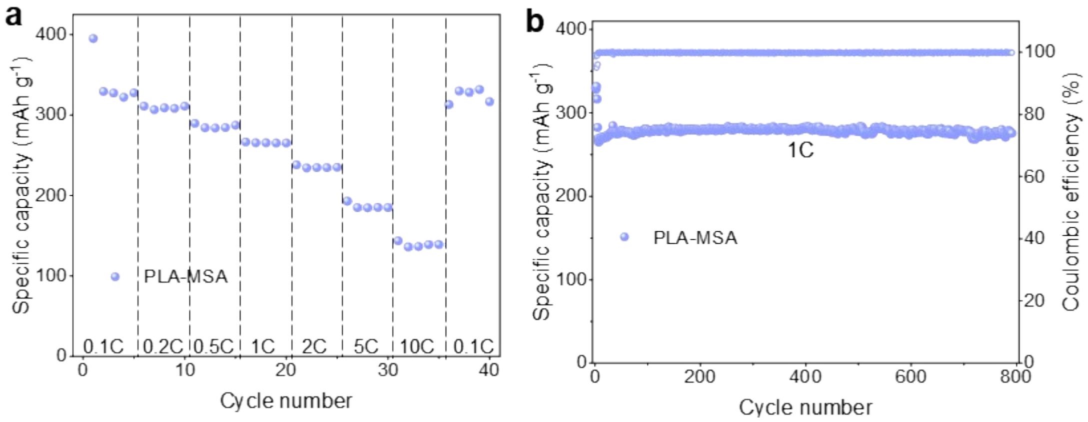

Fig. S42: (a) Rate performance and (b) cycling performance of PLA-MSA at 1C in half-cells.

Fig. S43: Industrial-Scale Preparation Engineering. Cotton fiber feedstock and MSA were first added into a large-scale corrosion-resistant industrial stirred reactor for mixing. The system was heated to 80°C; upon reaction completion, the mixture was separated (solid-liquid) and transferred to a large-scale industrial atmosphere sintering furnace. Under flowing argon, the furnace was heated to 1300°C, held isothermally for 3 h, and cooled naturally to yield kilogram-scale HC.

Table S1: Physical parameters of carbon materials

Sample	**d_{002}（nm）**	**Lc (nm)**	**$n=Lc/d_{002}+1$**	**La (nm)**	**Pore Volume ($cm^3\ g^{-1}$)**
COT	3.96	1.61	5.06	3.28	0.0281
COT-MSA	4.18	1.92	5.59	3.92	0.00217

Table S2: Comparison of the ICE and specific capacity of representative hard carbon anodes.

Hard carbon	Voltage range (V)	Initial coulombic efficiency (%)	Reversible capacity (mAh g^{-1})	Current density (mA g^{-1})	Ref	Electrolytes
CCL-HC	0-2.5	62.8	292	50	40	DME
CAC1300	0-2.5	82.3	308.4	30	41	EC/DEC
HTCNCC1500	0.-2.5	90.4	314	30	42	EC/DMC
CHC-0.25	0-2.0	82.8	324.6	20	43	EC/DMC
VCA-3	0-2.5	82.7	258	30	44	EC/DMC
CHC	0-2.0	68	341	20	45	PC/FEC
HCS-1300	0-2.5	73.6	304	30	46	EC/DMC
CCD-1300	0-2.5	91	300	30	47	EC/DMC
HC-1400	0-2.5	82.1	296.3	30	48	DME
RHC	0-2	91.45	320.96	50	9	DME
PCBC125	0-2	89.7	330.2	20	28	DME
COT-MSA	0-2.5	92.19	340.6	30	This work	DME
COT-MSA	0-2.5	87.2	331.6	30	This work	EC/DMC

Table S3: Inventory data of LCA for COT and COT-MSA.

Scenario case	Process	Unit	COT	COT-MSA
Inputs				
Pretreatment	Cotton	kg	8.33	3.48
	MSA	kg	N/A	69.52
	Water	kg		347.58
Pyrolysis	Biochar	kg	8.33	1.90
	Electricity	kW h	2.26	0.52
	Argon	kg	2.68	0.61
Outputs				
Pretreatment	Biochar	kg	8.33	1.90
	Waste water	kg	N/A	349.45
	Recycled MSA	kg		67.65
Pyrolysis	Carbon	kg	1	1
	Direct H_2O	kg	2.07	0.26
	Direct CH_4	kg	2.09	0.28
	Direct CO	kg	2.32	0.26
	Direct CO_2	kg	0.85	0.10
Performance ratio			0.66	0.83
capacity	372	mA h g^{-1}	245.26	306.95
FU		kg	1	1

Table S4: Environmental impact results of COT and COT-MSA for sodium-ion batteries.

Impact categories	Unit	COT	COT-MSA
acidification - acidification (incl. fate, average Europe total, A&B)	[10^{-2} kg SO_2-Eq]	72.73	28.70
climate change - global warming potential (GWP100)	[kg CO_2-Eq]	158.86	33.73
ecotoxicity: freshwater - freshwater aquatic ecotoxicity (FAETP inf)	[kg 1,4-DCB-Eq]	110.48	41.70
ecotoxicity: marine - marine aquatic ecotoxicity (MAETP inf)	×10^4 [kg 1,4-DCB-Eq]	6.56	2.81
ecotoxicity: terrestrial - terrestrial ecotoxicity (TETP inf)	[kg 1,4-DCB-Eq]	39.71	13.30
eutrophication - eutrophication (fate not incl.)	[10^{-2} kg PO4-Eq]	115.50	39.23
human toxicity - human toxicity (HTP inf)	[kg 1,4-DCB-Eq]	71.49	36.45
material resources: metals/minerals - abiotic depletion potential (ADP): elements (ultimate reserves)	[kg Sb-Eq]	0.00035	0.00029
ozone depletion - ozone layer depletion (ODP steady state)	[kg CFC-11-Eq]	7.1453E-07	3.79387E-07
photochemical oxidant formation - photochemical oxidation (high NOx)	[10^{-3} kg ethylene-Eq]	130.74	18.00